Tunable magnetic properties of monoatomic metal-oxide Fe/MgO multilayers

A. Kozioł-Rachwał,[1,*] T. Ślęzak,[1] K. Matlak,[1] P. Kuświk,[2] M. Urbaniak,[2] F. Stobiecki,[2] L. D. Yao,[3]
S. van Dijken,[3] and J. Korecki[1,4]

[1]*Faculty of Physics and Applied Computer Science, AGH University of Science and Technology, al. Mickiewicza 30, 30-059 Kraków, Poland*
[2]*Institute of Molecular Physics, Polish Academy of Sciences, ul. Mariana Smoluchowskiego 17, 60-179 Poznań, Poland*
[3]*NanoSpin, Department of Applied Physics, Aalto University School of Science, P.O. Box 15100, FI-00076 Aalto, Finland*
[4]*Jerzy Haber Institute of Catalysis and Surface Chemistry, Polish Academy of Sciences, ul. Niezapominajek 8, 30-239 Kraków, Poland*

Metal-oxide $[\mathrm{Fe}_K/(\mathrm{MgO})_L]_N$ multilayers were grown on MgO(001) substrates for various integer numbers (K,L) of the Fe(001) and MgO(001) monolayers, respectively, and the number of repetitions N varied from 6 to 30. Room-temperature conversion electron Mössbauer spectroscopy (CEMS) measurements proved that the magnetic properties of these monoatomic multilayers were extremely sensitive to both the Fe and MgO sublayer thicknesses. A stable ferromagnetic state and a strong perpendicular magnetization component at room temperature were obtained by changing the sublayer thickness and the number of multilayer repetitions. The analysis of the CEMS spectra in correlation with the magneto-optic Kerr effect measurements indicated a complicated domain structure in this special type of metal-insulator material. The vortexlike domain structure was confirmed by micromagnetic simulations.

I. INTRODUCTION

Since the first experimental evidence of perpendicular magnetic anisotropy (PMA) in ultrathin metallic films [1] and multilayers [2], research concerning the applications of PMA materials has intensified significantly. During the last three decades, PMA has been observed in many all-metal layered materials; for reviews, consult Refs. [3,4]. From the perspective of novel spintronics applications, the possibility of integrating the materials that exhibit PMA with semiconductor technology is still a challenge for future development. This is a nontrivial problem because of the diminished effectiveness of the spin injection between a metal and a semiconductor [5]. Recently, several groups have presented solutions to the conductivity mismatch by demonstrating spin injection into silicon from ferromagnetic metal through $\mathrm{Al_2O_3}$ [6], MgO [7], and graphene [8] tunnel barriers, which, when combined with PMA in a metal-oxide interface, as reported for $\mathrm{Pt/CoFe/AlO}_x(\mathrm{CrO}_x)$ [9], Co/Pt/oxide [10], and CoFeB/MgO [11], offer new prospects for semiconductor spintronics devices. On the other hand, metal-insulator layered [12,13] and granular [14] materials are attractive for tailoring not only magnetic but also transport properties.

Recently, we have demonstrated that iron in epitaxial MgO/Fe/MgO trilayers grown on MgO(001) has perpendicular anisotropy below a certain critical Fe thickness [15,16]; however, because of the cluster growth, superparamagnetism significantly influences the magnetic properties of MgO/Fe/MgO at room temperature (RT). Simultaneously, granular Fe/MgO multilayers fabricated on amorphous [13,17] and single-crystal substrates [18] have been optimized for maximum tunneling magnetoresistance (TMR) and field sensitivity at RT.

The goal of this study was to optimize the composition of the MgO/Fe multilayers to achieve stable magnetic properties

and perpendicular magnetization at RT. This goal was realized using a stack of alternating Fe and MgO sublayers with precisely selected thicknesses in the few-monolayer (ML) range. Although in this MgO thickness the TMR properties cannot be expected, the Fe/MgO multilayers have interesting magnetic properties related to the ferromagnetism of the ultrathin Fe sublayers. Whereas in a recent paper [19] we have shown that the problem of superparamagnetism can be circumvented via low-temperature growth, as proposed by Fahsold *et al.* [20], in the study reported here, we suppressed the superparamagnetism by exploiting the interlayer coupling in $(\mathrm{Fe}_K/\mathrm{MgO}_L)_N$ multilayers grown on single-crystal MgO(001) substrates, where the integers K and L indicate the nominal sublayer thickness in units of the numbers of atomic Fe(001) and MgO(001) geometrical monolayers (half the lattice constant for the body-centered-cubic [bcc] and face-centered-cubic [fcc] structures), which roughly correspond to 1.45 and 2.1 Å per monolayer, respectively, and N is the number of repetitions. Surprisingly, down to the thinnest studied Fe sublayers (3 ML), the metallic character of multilayers was preserved with no massive oxidation, as revealed via Mössbauer spectroscopy. By changing the Fe and MgO sublayer thicknesses, the magnetic properties— Curie temperature and magnetic anisotropy (MA)—could be sensitively tuned.

II. EXPERIMENTAL DETAILS

The $(\mathrm{Fe}_K/\mathrm{MgO}_L)_N$ multilayers, for $2 < K < 6$ and $1.5 < L < 5$, were grown via the alternate deposition of Fe and MgO under ultrahigh vacuum conditions at RT on 10-nm-thick homoepitaxial MgO(001) buffer layers deposited at 450 °C on polished MgO(001) substrates. Iron sublayers were deposited from a BeO crucible heated by wraparound tungsten coils embedded in a water-cooled shroud. Most of the samples were prepared with the ^{57}Fe isotope to enable Mössbauer spectroscopy studies. MgO layers were prepared using an electron beam evaporator (EBV). The thickness of the

_____
*Author to whom correspondence should be addressed: akoziol@agh.edu.pl
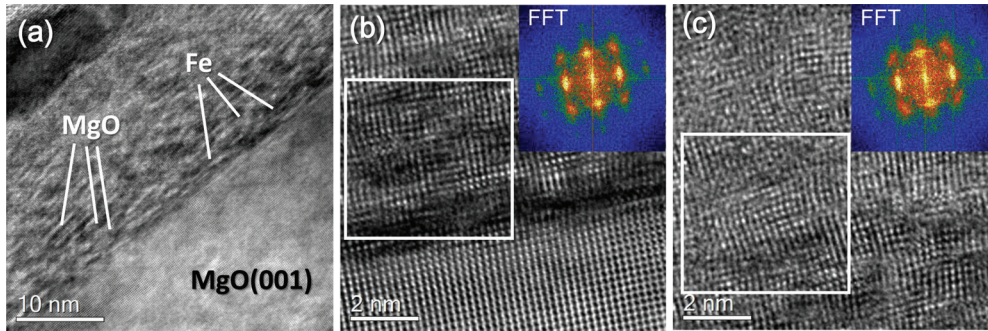
FIG. 1. (Color online) (a) Cross-sectional TEM image of a $(Fe_4/MgO_3)_{15}$ multilayer on MgO (001). (b) HRTEM image from a local area near the MgO substrate and the corresponding fast Fourier transform (FFT) pattern (inset). (c) HRTEM image and FFT pattern from an area more than 3 nm away from the MgO substrate. The (002) reflection arcs indicate that the orientation of the small Fe and MgO grains deviates from epitaxial growth.

sublayers was controlled using a quartz microbalance with an accuracy of approximately 10%. The samples were prepared for different repetition numbers of the Fe_K/MgO_L bilayers N in the $6 < N < 30$ range. The low-energy electron diffraction (LEED) pattern, which indicated typical epitaxial relations between the Fe(001) and MgO(001) for the initial stages of the multilayer growth, systematically worsened and finally vanished after the deposition of the third Fe/MgO bilayer. The microstructure of the as-prepared multilayers was analyzed by high-resolution transmission electron microscopy (HRTEM) on a JEOL 2200FS TEM with double Cs correctors. The cross-sectional TEM specimens were prepared by mechanical polishing and argon ion beam milling. Figure 1(a) shows a TEM image of a $(Fe_4/MgO_3)_{15}$ multilayer. Most of the multilayer is discontinuous, but alternating Fe and MgO sublayers can be detected in some local areas [indicated by white lines in Fig. 1(a)]. The HRTEM image of Fig. 1(b) illustrates the presence of a mosaic microstructure containing small regions of Fe and MgO. This structure becomes increasingly disturbed with an increasing number of Fe_4/MgO_3 bilayer repetitions [Fig. 1(c)]. Therefore, the multilayer parameters K, L, and N should be taken as nominal values, without any direct relation to the actual periodicity. All these TEM results are in good agreement with LEED analysis. The magnetic properties of the multilayers were characterized *ex situ* using conversion electron Mössbauer spectroscopy (CEMS) and the magneto-optic Kerr effect (MOKE). Conversion electron Mössbauer spectroscopy measurements were performed using a standard Mössbauer spectrometer equipped with a He/CH$_4$-flow proportional detector and a 100-mCi ^{57}Co(Rh) source. The CEMS spectra were collected in the normal-incidence geometry and fitted using commercial software by applying a Voigt-line-based method, in which the distribution of the hyperfine parameters is represented by a sum of Gaussian components [21].

III. RESULTS AND DISCUSSION

Ultrathin Fe(001) films embedded between the MgO(001), with thicknesses below the critical value necessary to establish perpendicular magnetization [15,16], are superparamagnetic at RT, as indicated in Fig. 2(a) by the CEMS spectrum of a 4-ML Fe film deposited at RT. The corresponding superparamagnetic

fluctuation frequency is on the order of 100 MHz, and it fits the characteristic time window when a Mössbauer spectrum is sensitive to dynamic processes (10^{-7}–10^{-9} s). The spectrum
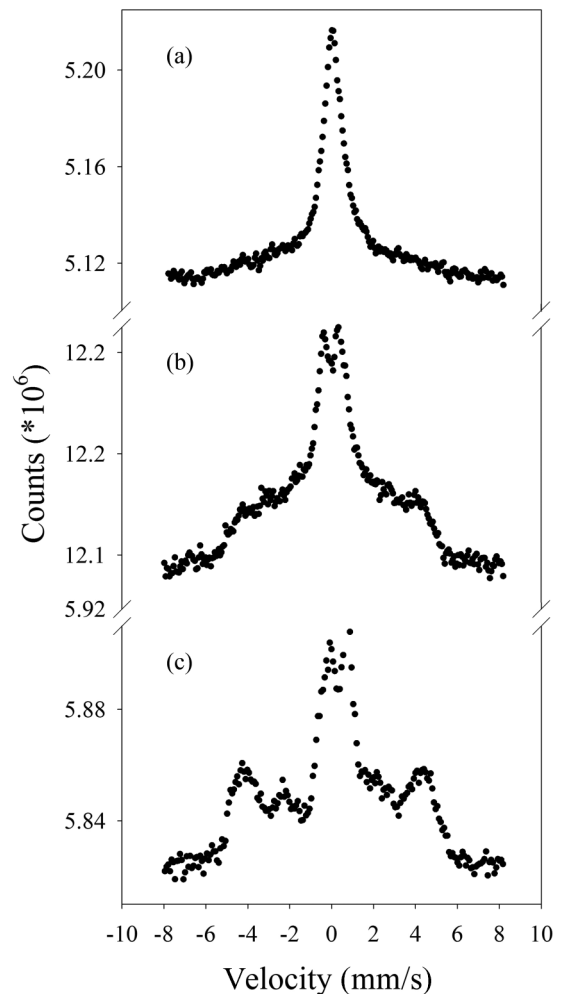

FIG. 2. RT conversion electron Mössbauer spectra of (a) a 4-ML layer of ^{57}Fe embedded between MgO layers, (b) a 4-ML layer of ^{57}Fe embedded between MgO layers in an external magnetic field of 0.15 T applied along the film normal, i.e., parallel to the γ ray direction, and (c) $(^{57}Fe_4/MgO_5)_{10}$ multilayers.

is characterized by a typical broadening that reveals that the ferromagnetic order is averaged out because of random jumps in the magnetization of the superparamagnetic particles. On the other hand, the fluctuation frequency misses the characteristic time window of magnetization measurements (e.g., MOKE) by many orders of magnitude, and using those methods, no magnetic order could be detected. A moderate external magnetic field of 0.15 T perpendicular to the film was able to partially suppress the superparamagnetism, which manifested in the spectrum as the onset of the magnetic splitting of the single line [Fig. 2(b)]. A similar effect could be achieved by stacking several Fe layers separated by ultrathin MgO. An exemplary spectrum for $(Fe_4/MgO_5)_{10}$ multilayers is shown in Fig. 2(c). Without going into the details of the spectrum interpretation, it is obvious that the exchange coupling between the Fe sublayers partially stabilizes the superparamagnetic fluctuations for the MgO sublayers with a thickness of 5 ML in a similar manner as an external magnetic field. This observation paved the way for tuning the magnetic properties of the monoatomic Fe/MgO multilayers by optimizing their composition.

In the course of the optimization, it was found that the magnetic properties of the superlattices—the superparamagnetic blocking temperature and the MA—are very sensitive to the Fe and MgO sublayer thicknesses and the repetition number. The thinner the Fe sublayers were, the stronger the perpendicular anisotropy was; on the other hand, to stabilize the long-range magnetic order for the thinnest Fe, the MgO sublayers also had to be kept sufficiently thin. However, for an MgO thickness of less than 3 ML, the in-plane magnetization dominated, which we interpreted as an effect of the direct pinhole-mediated ferromagnetic coupling. The perpendicular anisotropy could also be tuned by changing the repetition number N. Finally, multilayers with $K = 4$ and $L = 3$, i.e., $(Fe_4/MgO_3)_N$, were selected for the detailed analysis.

Figures 3(a)–3(c) show experimental CEMS spectra (points) collected for $(Fe_4/MgO_3)_N$ multilayers with $N = 10$, 15, and 20, respectively. The well-resolved six-line patterns with broadened lines for all spectra reveal a static long-range magnetic order. The most prominent change in the spectra with increasing N is the decrease in intensity of the second and fifth lines of the sextet, which signifies a change in the magnetization direction toward the film normal, which is discussed below with respect to the numerical analysis of the spectra.

All spectra were consistently fitted within a model that is adequate to the nominal multilayer stack structure of the ultrathin Fe sublayers. Previous studies of ultrathin Fe(001) films embedded in MgO using hyperfine interaction spectroscopy, CEMS [15], and nuclear resonance scattering of synchrotron radiation [16] have shown that the hyperfine pattern of a single Fe film can be well described by a narrow distribution of the hyperfine magnetic field (B_{HF}), an isomer shift (IS) and a small quadrupole interaction (QS). A similar subspectrum, henceforth referred to as the "site", in which the distributions of the hyperfine parameters were sums of Gaussians, was used to describe the given Fe sublayer. Additionally, to account for structural and morphological changes in the consecutive Fe sublayers, which are obvious from the vanishing LEED pattern and from the TEM analysis, multiple sites, each represented
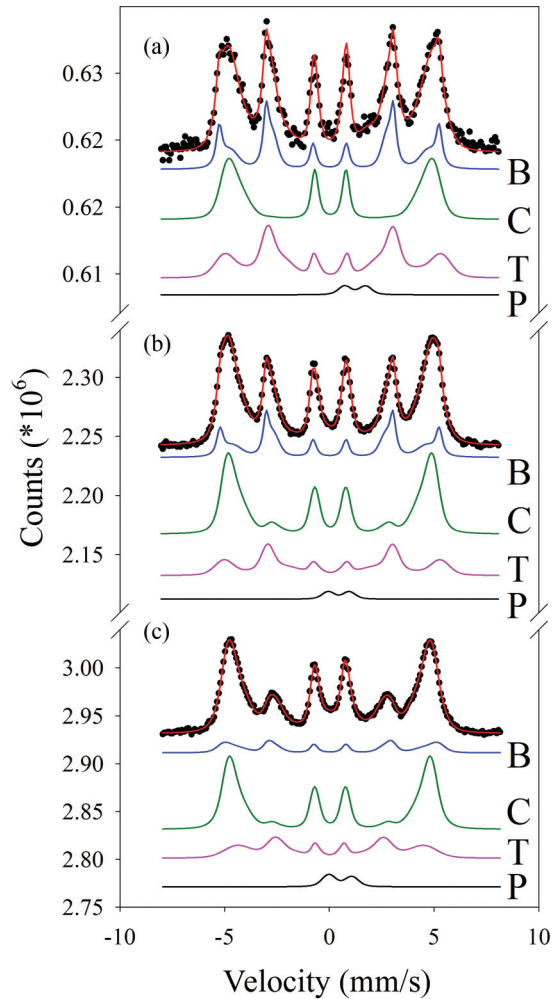

FIG. 3. (Color online) CEMS spectra (black points) and the results of the best fits (red lines) of $(Fe_4/MgO_3)_N$ stacks with (a) $N = 10$, (b) $N = 15$, and (c) $N = 20$. The fits were deconvoluted into sites B, C, T, and P.

by a subspectrum, were allowed. Ideally, the number of these sites should correspond to the number of sublayers, but we found in practice that satisfactory fits were obtained using three magnetic sites that reflected properties of the film regions situated at different depths of the multilayer samples: site B describes the most-buried (Fe_4/MgO_3) bilayers, site C represents the central part, and site T represents the topmost region of the multilayers. Additionally, a small-intensity paramagnetic site P was identified in all spectra, and based on the hyperfine parameters, it was attributed to ferric irons in the MgO matrix [22,23]. The relative intensities of the subspectra B, C, and T and some spectral features for the superlattices with different N are depicted in Fig. 4. The P site is neglected in this representation due to its very small contribution (the contribution of the P site was varying from 2% for $N = 10$ to 5% for $N = 20$).

The magnetic sites have bimodal distributions of the hyperfine magnetic field B_{HF}. The narrower component of the hyperfine magnetic field, which has a higher average value (B_{HF1}), represents the Fe atoms in the central part of the given Fe sublayer. The broader component, whose average value B_{HF2}
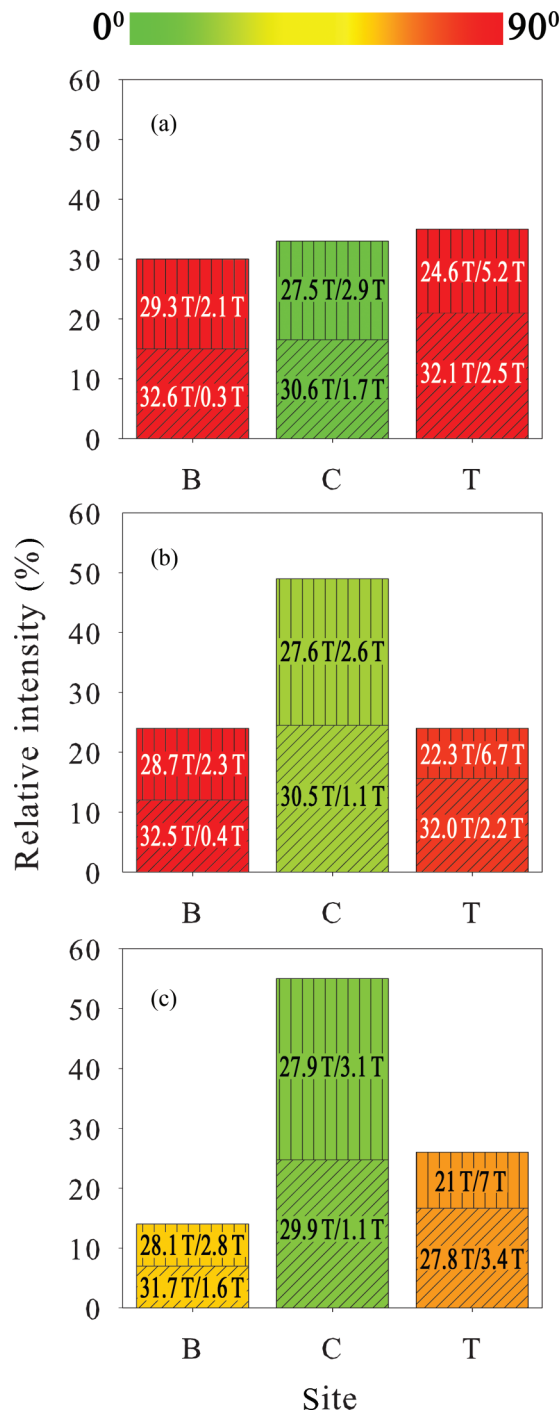
FIG. 4. (Color online) The relative intensity of sites (B, C, T) derived from the numerical fits of the CEMS spectra for the (Fe$_4$/MgO$_3$)$_N$ stacks with different numbers of repetitions N: (a) $N = 10$, (b) $N = 15$, (c) $N = 20$. Contributions of the components, which represent the central and interfacial atoms in the Fe sublayers are marked by the diagonal and vertical hatch, respectively. Values of B_{HF1} and B_{HF2} together with their distribution widths are noted in the corresponding areas. The color scale shows the average Fe spin angle relative to the incident γ rays.

is lower than B_{HF1}, represents the Fe atoms at the Fe/MgO interface. This component assignment follows the general trend that we have previously observed at defect-containing

Fe/MgO interfaces [24,25]. All the magnetic sites have slightly positive ISs, which can be related to the *s*-electron transfer from iron to oxygen [26]. No sites characteristic of bulk Fe oxides, which have much more positive IS values, were observed. The intensities of the components which describe central and interface atoms are marked in Fig. 4 by the area with the diagonal and vertical hatch, respectively. The values of B_{HF1} and B_{HF2} and their distribution widths are noted in the corresponding areas.

The key fit parameter was the intensity ratio R of the second (or fifth) to the third (or fourth) line of the sextet that described a given site, $R = I_{2(5)}/I_{3(4)}$. The R value is sensitive to the angle θ between the hyperfine magnetic field (local magnetization) and the γ ray direction: $R = 4\sin^2\theta/(1 + \cos^2\theta)$. For the given CEMS geometry (γ rays along the film normal), the magnetization direction is uniquely defined for the perpendicular ($\theta = 0°$, $R = 0$) and in-plane ($\theta = 90°$, $R = 4$) orientations; otherwise, similar θ values may result from different distributions of the magnetization direction. For example, in the case of a random distribution of the magnetic hyperfine field directions, $R = 3$, and the same value results when $\theta = 68°$.

For sites B and T, which correspond to the outer Fe sublayers, θ is close (or equal) to 90°, which means that they are in-plane magnetized (see color scale in Fig. 4). In contrast, the central layers described by site C are characterized by small angles θ, i.e., their magnetization is nearly perpendicular. The relative spectral intensity of site B is 30%, 24%, or 14% for $N = 10$, 15, or 20, respectively, which corresponds to the contributions from three Fe sublayers of the (Fe$_4$/MgO$_3$)$_N$ stack, equal for each N. The intensity of the component C increases with increasing N, which is clearly reflected in the spectra in the decreasing intensities of the second and fifth lines, as can be distinctly seen in the spectrum for $N = 20$. Site T, with relative weights of 35%, 24%, and 26% for $N = 10$, 15, and 20, respectively, is characterized by a broad distribution of B_{HF2}. This is a consequence of the increased interface mixing between the Fe and MgO.

The validity of the above spectrum interpretation was supported by additional CEMS measurements using a ^{57}Fe probe sublayer embedded during growth at the defined depth in the multilayer, which was otherwise composed of the non-Mössbauer ^{56}Fe. Similar methodology was used by Hamada *et al.* [27] to study the evolution of magnetic structure in Co/Au multilayers. Figure 5(a)–5(c) shows the measured spectra for (^{56}Fe$_4$/MgO$_3$)$_{10}$ with the ^{57}Fe$_4$ probe sublayer placed directly on the MgO(001) substrate, in the center of the multilayer and on the top, respectively. All these spectra contain significant paramagnetic components, with values of IS and QS that are characteristic of Fe^{2+} and Fe^{3+} in a MgO matrix. The increased contribution of nonmagnetic components in comparison with the previously described spectrum of (Fe$_4$/MgO$_3$)$_{10}$ [Fig. 3(a)] is related to the slightly different thickness of the MgO sublayers in the stack. The intensity ratio R of the second (or fifth) to the third (or fourth) line was determined to be 2.0 for both the deepest and topmost Fe sublayers, whereas $R = 1.27$ for the central sublayer. The comparison of the corresponding R values proves that the out-of-plane magnetization component is most developed in the center of the multilayer. In addition, the broadening of the
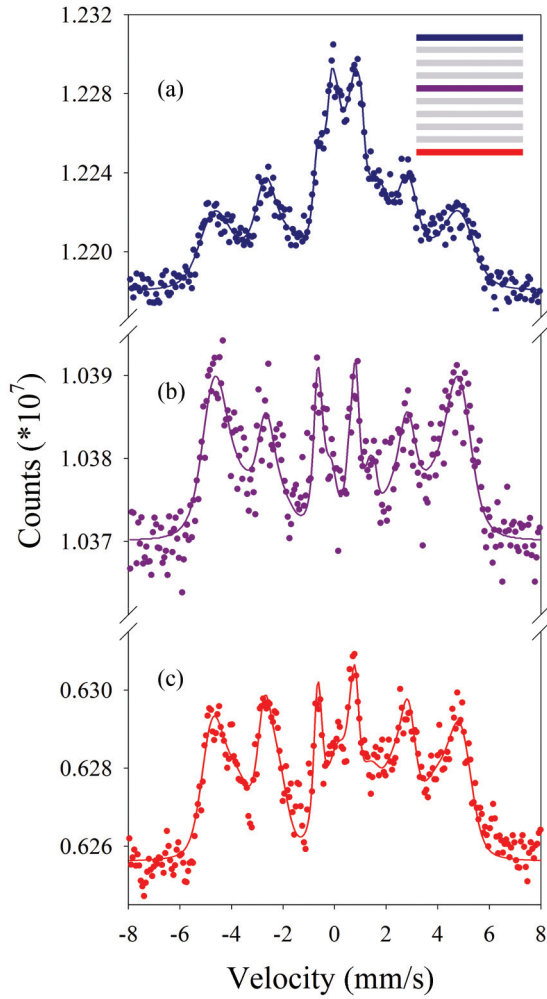
FIG. 5. (Color online) CEMS spectra of $(^{56}Fe_4/MgO_3)_{10}$. The 4-ML ^{57}Fe probe layer was deposited at various depths. The inset scheme shows the position of the probe layer in the stack for each depicted spectrum.

B_{HF} distribution increases as the distance of the ^{57}Fe probe from the MgO(001) substrate increases, which confirms the perturbation of the structure and periodicity.

The analysis of the CEMS spectra suggests a complex magnetization structure in the (Fe/MgO) multilayers, which is also reflected in the hysteresis loops measured via MOKE. Figure 6 shows the hysteresis loops measured for $(Fe_4/MgO_3)_N$ in the perpendicular (PMOKE) and longitudinal (LMOKE) configurations as a function of N. In the LMOKE signal, we observed a gradual decrease of the remanence with increasing N, to about 60%, 50%, and 10% for $N = 10$, 15, and 20, respectively. Simultaneously, a small hysteresis appeared in the PMOKE signal (see the insets in Fig. 6) with the coercive field of about 10 mT for $N \geqslant 15$.

Similar MOKE loops were observed by Tekielak *et al.* [28] for Co/Au multilayers. They were explained in terms of the interplay between the magnetostatic interactions and the out-of-plane anisotropy, which results in the magnetization distribution described by a vortexlike domain structure.

To elucidate the magnetization distribution in our system, micromagnetic simulations were performed with the OOMMF
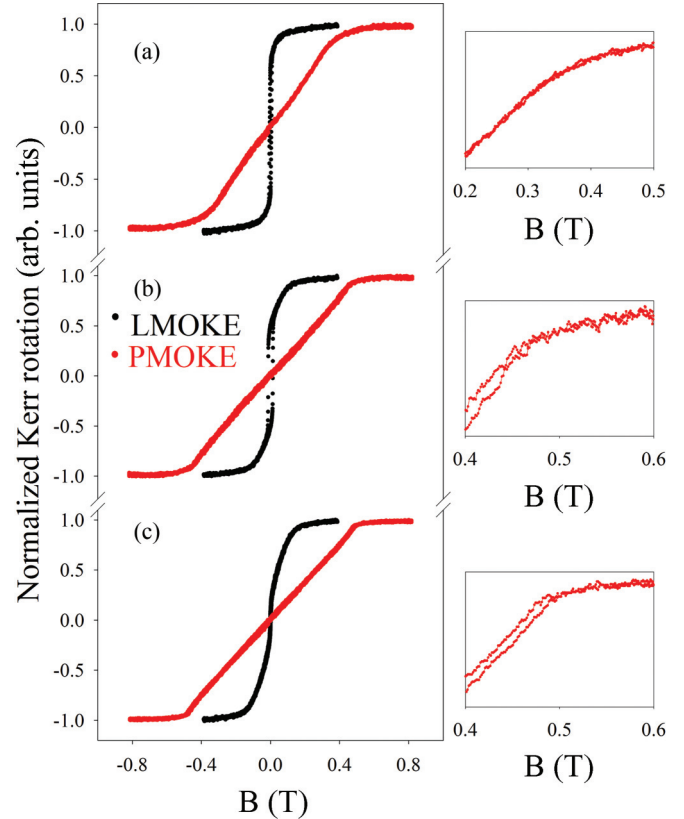

FIG. 6. (Color online) PMOKE and LMOKE hysteresis loops measured for $(Fe_4/MgO_3)_N$ for different numbers of repetitions: (a) $N = 10$, (b) $N = 15$, and (c) $N = 20$.

package [29]. The calculations were made for a slab with the volume of $(10\,000 \times 10\,000 \times 12)$ nm^3. The discretization cell size was chosen to be $(3 \times 10\,000 \times 0.6)$ nm^3 (see Fig. 7). The simulations were performed starting from the saturation along the z direction. The thicknesses of the Fe (d_{Fe}) and MgO (d_{MgO}) layers used in calculations were both equal to 6 Å, and the repetition number of the Fe/MgO stack was fixed to $N = 10$. To limit the number of the critical simulation parameters, for the Fe sublayers, we used the exchange stiffness and the saturation magnetization of bulk iron: $A_{Fe} = 21 \times 10^{-12}$ J/m and $M_s^{Fe} = 1.71 \times 10^6$ A/m, respectively. With these assumptions, the decisive parameters for the magnetization distribution were the effective MA and the interlayer exchange coupling (IEC). As shown in our
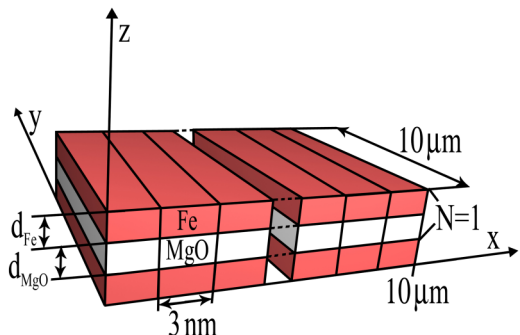

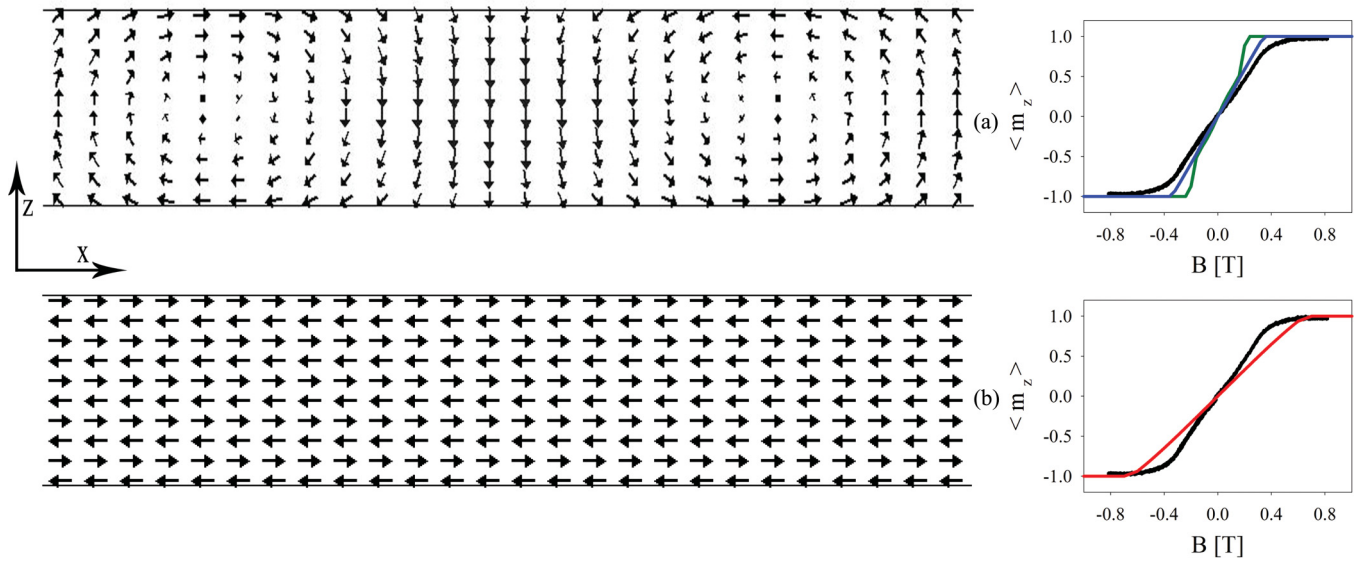FIG. 7. (Color online) Sample and cells used in simulations.

FIG. 8. (Color online) Simulated magnetic moment distribution at remanence (left panel) and the magnetization curves (right panel) obtained from the micromagnetic simulations for (Fe-0.6 nm/MgO-0.6 nm)$_{10}$ with different magnetic parameters: (a) $J = -0.1 \times 10^{-4}$ J/m^2 and $K_{eff} = -0.18$ MJ/m^3(green line) and $K_{eff} = -0.28$ MJ/m^3(blue line); and (b) $J = -0.5 \times 10^{-4}$ J/m^2 and $K_{eff} = -0.28$ MJ/m^3 (red line), compared with PMOKE hysteresis loop (black curves) from Fig. 6(a).

recent paper [19], the effective MA in the ultrathin Fe layers embedded between MgO results from the competition between the negative (the shape and magnetocrystalline anisotropy that favor in-plane magnetization) and positive terms (the magnetoelastic and surface anisotropy). This competition results in a weak effective MA constant K_{eff}, and it was shown by Tekielak *et al.* [28] and Labrune and Thiaville [30] that the vortexlike structure and zero remanence out-of-plane magnetization curves are expected when $K_{eff} < 0$.

Interlayer exchange coupling between the Fe sublayers interspersed with the MgO sublayers in the examined thickness range should be considered as either ferro- or antiferromagnetic (AFM), depending on the quality of the Fe/MgO interfaces [31,32], i.e., structural relaxation, presence of defects, etc. Our recent study of IEC in the Fe/MgO/Fe stack proved the existence of the AFM coupling between the Fe layers for monolayer MgO thicknesses [33].

The simulations showed that the magnetic structure is very sensitive to the combination of the K_{eff} and IEC coupling constant values J. The magnetization structure changes between the AFM in-plane alignments of the sublayer magnetizations and the vortexlike structure. The existence of the vortex structure, which well explains the observed experimental features, was confirmed by simulation for $K_{eff} \geqslant -0.28$ MJ/m^3 and $J = -0.1 \times 10^{-4}$ J/m^2, as shown in Fig. 8(a). It is worth noticing that, with the increasing negative K_{eff} value, the vortex structure gradually transforms to a stripe domain structure.

The vortex cores, magnetized in plane along the y axis, are separated from each other by perpendicularly magnetized areas. In the surface regions, the in-plane magnetized (along the x axis) antiparallel states are developed, with the in-plane x-magnetization component varying with a period of 138 and

94 nm for $K_{eff} = -0.18$ and -0.28 MJ/m^3, respectively. Figure 8(a) right, shows the volume-averaged out-of-plane magnetization component ($\langle m_z \rangle$) simulated for the magnetic field applied perpendicular to the surface. In a good agreement with the measured PMOKE loop for $N = 10$, the simulated magnetization has no hysteresis and a high saturation field.

The vortex domain structure has the magnetostatic origin. Whereas the MA favors the in-plane magnetization in individual sublayers, in the presence of the magnetostatic dipole interaction some magnetic moments in the vortex are pulled out of plane. If the AFM coupling between Fe sublayers is weak, the exchange energy term is dominated by the magnetostatic interaction, and the total energy is minimized by the vortex structure [Fig. 8(a)].

For the stronger AFM coupling ($J = -0.5 \times 10^{-4}$ J/m^2), the magnetization curves are similar [Fig. 8(b)], but the magnetization structure differs drastically: the Fe sublayers are aligned antiferromagnetically in plane.

Both the CEMS data, which reveal locally pronounced perpendicular magnetization component (the Mössbauer spectra are insensitive to the magnetization direction along z axis) and the polar Kerr loops, which show zero remanent magnetization, are then consistent with the vortex domain structure. This domain structure explains also the nonzero remanent magnetization in the LMOKE curves related to the m_y component of the vortex cores [28].

IV. CONCLUSIONS

Fe/MgO monoatomic metal-oxide multilayers grown on MgO(001) were tuned to a stable ferromagnetic state by optimizing the thicknesses of their components and the repetition number of the Fe/MgO bilayers. For (Fe$_4$/MgO$_3$)$_N$ multilayers with a perturbed periodicity, Mössbauer

measurements demonstrated that the out-of-plane magnetization component was enhanced when the repetition number N was increased from 10 to 20. From CEMS measurements with ^{57}Fe monolayer probes located at different sublayers, the perpendicular magnetization was found to be localized in the center of the multilayer, whereas in the exterior sublayers, in-plane magnetization dominated. Correlations between the CEMS and MOKE measurements suggest a complex vortexlike magnetization distribution. Plausibility of this domain structure was confirmed by the micromagnetic simulations.

[1] U. Gradmann and J. Müller, Phys. Status Solidi **27**, 313 (1968).

[2] P. F. Carcia, A. D. Meinhaldt, and A. Suna, Appl. Phys. Lett. **47**, 178 (1985).

[3] M. T. Johnson, P. J. H. Bloemen, F. J. A. den Broeder, and J. J. de Vries, Rep. Prog. Phys. **59**, 1409 (1996).

[4] C. A. F. Vaz, J. A. C. Bland, and G. Lauhoff, Rep. Prog. Phys. **71**, 056501 (2008).

[5] E. I. Rashba, Phys. Rev. B **62**, R16267 (2000).

[6] B. T. Jonker, G. Kioseoglou, A. T. Hanbicki, C. H. Li, and P. E. Thompson, Nat. Phys. **3**, 542 (2007).

[7] T. Sasaki, T. Oikawa, T. Suzuki, M. Shiraishi, Y. Suzuki, and K. Noguchi, IEEE Trans. Magn. **46**, 1436 (2010).

[8] O. M. J. van't Erve, A. L. Friedman, E. Cobas, C. H. Li, A. T. Hanbicki, K. M. McCreary, J. T. Robinson, and B. T. Jonker, J. Appl. Phys. **113**, 17C502 (2013).

[9] S. Monso, B. Rodmacq, S. Auffret, G. Casali, F. Fettar, B. Gilles, B. Dieny, and P. Boyer, Appl. Phys. Lett. **80**, 4157 (2002).

[10] L. E. Nistor, B. Rodmacq, S. Auffret, and B. Dieny, Appl. Phys. Lett. **94**, 012512 (2009).

[11] S. Ikeda, K. Miura, H. Yamamoto, K. Mizunuma, H. D. Gan, M. Endo, S. Kanai, J. Hayakawa, F. Matsukura, and H. Ohno, Nat. Mater. **9**, 721 (2010).

[12] M. Nakamura, D. Okuyama, J. S. Lee, T. Arima, Y. Wakabayashi, R. Kumai, M. Kawasaki, and Y. Tokura, Adv. Mater. **22**, 500 (2010).

[13] A. García-García, J. A. Pardo, E. Navarro, P. Štrichovanec, A. Vovk, L. Morellón, P. A. Algarabel, and M. R. Ibarra, Appl. Phys. A **107**, 871 (2012).

[14] B. Abeles, in *Applied Solid State Science: Advances in Materials and Device Research*, edited by R. Wolfe (Academic, New York, 1976), p. 1.

[15] J. Balogh, I. Dézsi, Cs. Fetzer, J. Korecki, A. Kozioł-Rachwał, E. Młyńczak, and A. Nakanishi, Phys. Rev. B **87**, 174415 (2013).

[16] A. Kozioł-Rachwał, T. Giela, B. Matlak, K. Matlak, M. Ślęzak, T. Ślęzak, M. Zając, R. Rüffer, and J. Korecki, J. Appl. Phys. **113**, 214309 (2013).

[17] A. García-García, A. Vovk, J. A. Pardo, P. Štrichovanec, C. Magén, E. Snoeck, P. A. Algarabel, J. M. De Teresa, L. Morellón, and M. R. Ibarra, J. Appl. Phys. **105**, 063909 (2009).

[18] A. García-García, J. A. Pardo, P. Štrichovanec, C. Magén, A. Vovk, J. M. De Teresa, G. N. Kakazei, Y. G. Pogorelov, L. Morellón, P. A. Algarabel, and M. R. Ibarra, Appl. Phys. Lett. **98**, 122502 (2011).

[19] A. Kozioł-Rachwał, W. Skowroński, T. Ślęzak, D. Wilgocka-Ślęzak, J. Przewoźnik, T. Stobiecki, Q. H. Qin, S. van Dijken, and J. Korecki, J. Appl. Phys. **114**, 224307 (2013).

[20] G. Fahsold, A. Pucci, and K.-H. Rieder, Phys. Rev. B **61**, 8475 (2000).

[21] K. Lagarec and D. G. Rancourt, Nucl. Instr. Meth. B **129**, 266 (1997).

[22] S. G. Marchetti, R. Spretz, M. A. Ulla, and E. A. Lombardo, Hyperfine Interact. **128**, 453 (2000).

[23] A. Perez, G. Marest, B. D. Sawicka, J. A. Sawicki, and T. Tyliszczak, Phys. Rev. B **28**, 1227 (1983).

[24] E. Młyńczak, K. Freindl, N. Spiridis, and J. Korecki, J. Appl. Phys. **113**, 024320 (2013).

[25] M. Zając, K. Freindl, K. Matlak, M. Ślęzak, T. Ślęzak, N. Spiridis, and J. Korecki, Surf. Sci. **601**, 4305 (2007).

[26] H. Akai, S. Blügel, R. Zeller, and P. H. Dederichs, Phys. Rev. Lett. **56**, 2407 (1986).

[27] S. Hamada, N. Hosoito, T. Ono, and T. Shinjo, J. Magn. Magn. Mater. **198-199**, 496 (1999).

[28] M. Tekielak, R. Gieniusz, M. Kisielewski, P. Mazalski, A. Maziewski, V. Zablotskii, F. Stobiecki, B. Szymański, and R. Schäfer, J. Appl. Phys. **110**, 043924 (2011).

[29] M. J. Donahue and D. G. Porter, OOMMF User's Guide, Version 1.0 (1999), http://math.nist.gov/oommf/.

[30] M. Labrune and A. Thiaville, Eur. Phys. J. B **23**, 17 (2001).

[31] T. Katayama, S. Yuasa, J. Velev, M. Ye. Zhuravlev, S. S. Jaswal, and E. Y. Tsymbal, Appl. Phys. Lett. **89**, 112503 (2006).

[32] H. X. Yang, M. Chshiev, A. Kalitsov, A. Schuhl, and W. H. Butler, Appl. Phys. Lett. **96**, 262509 (2010).

[33] A. Kozioł-Rachwał, T. Ślęzak, M. Ślęzak, K. Matlak, E. Młyńczak, N. Spiridis, and J. Korecki, J. Appl. Phys. **115**, 104301 (2014).